Welding Thin Plates of Aluminum Alloys— A Quantitative Heat-Flow Analysis

Experimentally observed thermal cycles are in agreement with computer heat-flow model calculations

BY S. KOU, T. KANEVSKY AND S. FYFITCH

ABSTRACT. Bead-on-plate, full-penetration, gas tungsten-arc welding was carried out in thin plates of commercial aluminum alloys, including 6061, 5052, 2014 and 7075. The workpiece was thermally insulated from specially designed fixtures to avoid heat sinks during welding. An automatic arc voltage controller, capable of maintaining arc voltages within ± 0.1 volt of the desired values, was employed, and the arc heat input was accurately controlled.

Thermal measurements inside, as well as outside, the fusion zone were conducted, and information regarding the degree of liquid pool convection was obtained. A computer heat flow model, which takes into account the heat of fusion, the convection of the weld pool, the size and distribution of the heat source, the temperature dependence of thermal properties and the heat loss from the surface of the workpiece, was developed. The experimentally observed thermal cycles, widths of the fusion zone and weld microstructures agreed very well with the calculated results, thus verifying the validity of such a welding heat flow model.

In order to make the results of welding heat flow studies more general, dimensionless variables were introduced. Also, the results of this study were presented and discussed using such dimensionless variables.

Introduction

The fusion welding of thin plates has been used frequently as a simple tool for studying the effects of welding heat input on the structure and properties of engineering materials. The understanding of the heat flow during thin-plate welding can make such studies both more quantitative and more systematic.

The analytical solution to the steady state, 2-dimensional heat flow problem involving the bead-on-plate, full-penetration welding of thin plates was first derived by Rosenthal (Ref. 1) in 1941. The major assumptions made were:

1. A point heat source.
2. No heat of fusion.
3. No surface heat loss due to convection or radiation.
4. Constant thermal properties of the workpiece material.

Many subsequent investigators (Ref. 2-10) have tried either to modify or to verify such an analytical solution. However, major improvements over Rosenthal's original theory have not been achieved until the recent application of numerical methods in the simulation of heat flow during thin-plate welding (Ref. 11-13).

In the present study, attempts were made to verify, under carefully controlled heat flow conditions during welding, the validity of the heat flow model developed. Such a model takes into account the size and distribution of the heat source, the heat of fusion, the convection of the weld pool, the surface heat loss due to convection and radiation, and the temperature dependence of thermal properties.

Commercial aluminum alloys of practical welding applications, such as 6061 and 5052, were employed. Alloys 2014 and 7075, although less weldable in practical situations, were also included due to their readily available information on weld microstructures.

Theory

The theory of the steady-state, 2-dimensional welding heat flow has been described in details elsewhere (Ref. 13) and thus is mentioned only very briefly here. In short, the heat flow equation can be written in terms of a coordinate system (x,y), which moves with the heat source at the same velocity (see Fig. 1). In other words:

$$0 = \frac{\partial}{\partial x}\left(k\frac{\partial T}{\partial x}\right) + \frac{\partial}{\partial y}\left(k\frac{\partial T}{\partial y}\right) + Q_v + U\frac{\partial(\rho H)}{\partial x}$$

where T is temperature, k the thermal conductivity, Q_v the volumetric heat source or sink, U the welding velocity, ρ the density and H the specific enthalpy of the workpiece material. The boundary

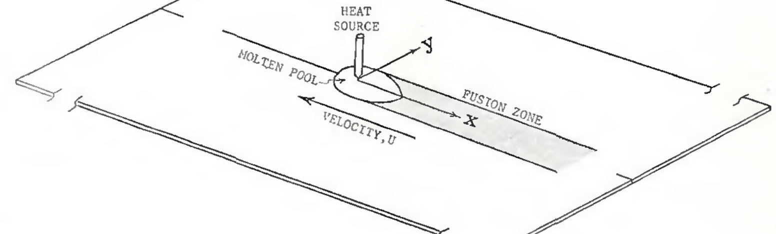

Fig. 1 — The schematic illustration of a pair of thin plates being butt welded with a heat source of constant velocity U

Paper presented at the 62nd AWS Annual Meeting held in Cleveland, Ohio, during April 5-10, 1981.

S. KOU is Assistant Professor and T. KANEVSKY is a Graduate Student, Department of Metallurgical Engineering and Materials Science, Carnegie-Mellon University, Pittsburgh, Pennsylvania, and S. FYFITCH, a former graduate student, is with Westinghouse Electric Corporation, Pittsburgh, Pennsylvania.

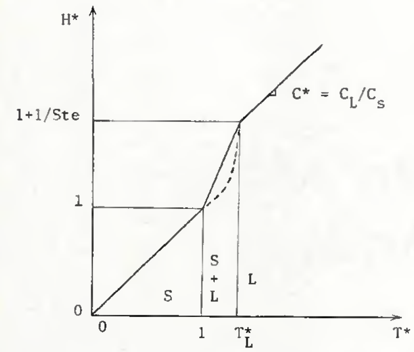

Fig. 2 — The thermodynamic relationship between the dimensionless enthalpy H and the dimensionless temperature T* in the solid phase (S), the liquid phase (L) and the mushy zone (S + L). The dashed line in the mushy zone indicates a possible nonlinear H* vs. T* relationship due to a nonlinear temperature vs. fraction liquid relationship*

conditions are:

$$T = T_o \text{ as } x \rightarrow \pm \infty$$

$$\frac{\partial T}{\partial y} = 0 \text{ at } y = \pm w/2$$

where T_o and w are the original temperature and the width of the workpiece.

In order to make the results of welding heat flow studies more general, dimensionless variables are adopted here. Listed below are the definitions of the dimensionless variables used in this study:

$H^* = (H-H_o)/(T_s-T_o)C_s$ .... dimensionless enthalpy.
$T^* = (T-T_o)/(T_s-T_o)$ .... dimensionless temperature.
$T_L^* = (T_L-T_o)/(T_s-T_o)$ .... dimensionless liquidus temperature.
$Ste = C_s(T_s-T_o)/\Delta H$.............. Stephan number.
$C^* = C/C_s$ .... dimensionless specific heat.

where H_o is the specific enthalpy at temperature T_o, T_s the solidus temperature, C_s the specific heat of the solid phase, T_L the liquidus temperature and ΔH the heat of fusion.

The above dimensionless variables describe the thermodynamic relationship between the enthalpy and the temperature of the material. Such a relationship is illustrated in Fig. 2. Although the heat flow model developed takes into account the temperature dependence of thermal properties (Ref. 13), this was not necessary for the present study, since the thermal properties of aluminum alloys do not vary significantly with temperature.

In addition to those listed above, the following dimensionless variables were also needed in the heat flow calculation:

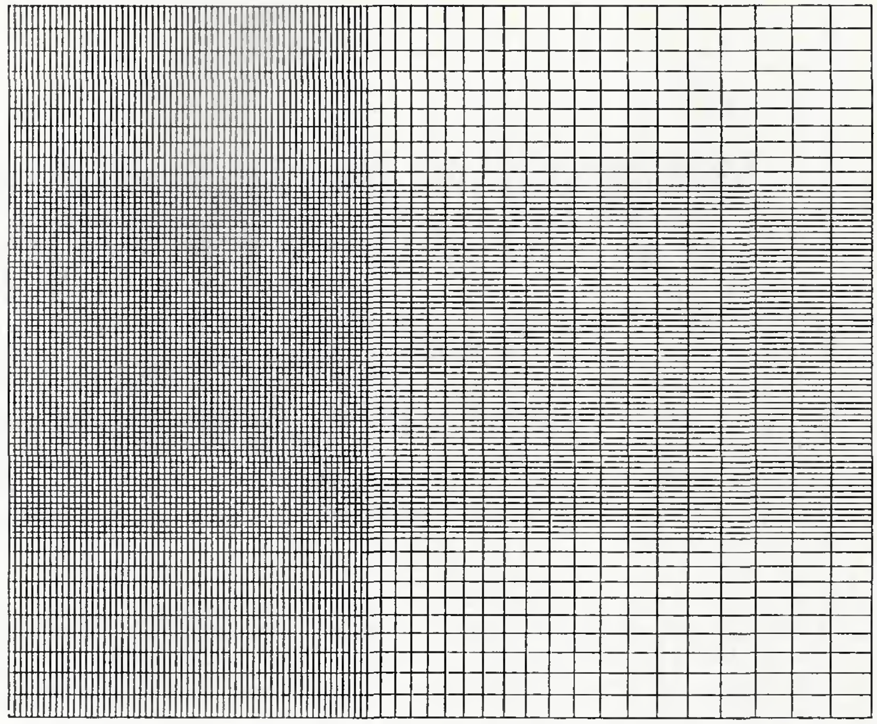

Fig. 3 — The grid mesh (41 by 81) used for simulating heat flow during thin plate welding. The grid spacing increases in an exponential function of the distance from the origin (the location of the heat source)

$Q^* = Q/(T_s-T_o)gk_s$ .... dimensionless heat input.
$Bi = h_{eff}\alpha_s^2/U^2gk_s$ .... Biot number.
$k^* = k/k_s$ .... dimensionless thermal conductivity.
$x^* = xU/\alpha_s$ .... dimensionless distance.
$y^* = yU/\alpha_s$ .... dimensionless distance.
$a^* = aU/\alpha_s$ .... dimensionless radius of heat source.
$w^* = wU/\alpha_s$ .... dimensionless width of workpiece.

where Q is the net heat input, g the thickness of the workpiece, k_s the thermal conductivity of the solid phase, h_{eff} the effective heat transfer coefficient due to convection and radiation, α_s the thermal diffusivity and a the radius of the heat source.

The relationship between Q and Q_v has been given elsewhere (Ref. 13). With the help of the above dimensionless variables, the heat flow equation and the boundary conditions were rewritten as follows:

Enthalpy Equation:

$$\oint k^* \left(\frac{\partial T^*}{\partial x^*}\vec{i} + \frac{\partial T^*}{\partial y^*}\vec{j}\right) d\vec{\ell}^* + Q^* + \int\int \frac{\partial H^*}{\partial x^*} dx^*\, dy^* = 0$$

Boundary Conditions:

$$T^* = 0 \text{ as } x^* \rightarrow \pm \infty$$

$$\frac{\partial T^*}{\partial y^*} = 0 \text{ at } y^* = \pm w^*/2$$

The above equations were broken down into the finite difference form and solved for the dimensionless temperature. Figure 2 was then used to find the corresponding dimensionless enthalpy needed for the next iteration of temperature calculation. Such calculations were repeated until the absolute value of the difference between the new and old values of the dimensionless temperature in two subsequent iterations became less or equal to 0.001, which corresponds to about 0.5°C.

The finite difference grid system used in this study is shown in Fig. 3. The center of the heat source, i.e., the origin of the coordinate system, coincided with the center of the area occupied by those very tiny squares. Since highest temperature gradients were expected near the heat source, very small grid spacings were used in order to gain better accuracy in calculations. However, farther away from the heat source, temperature gradients decreased and coarser grid spacings were used in order to cut down the storage and the computation time required.

Experimental Procedure

Commercial aluminum alloys including

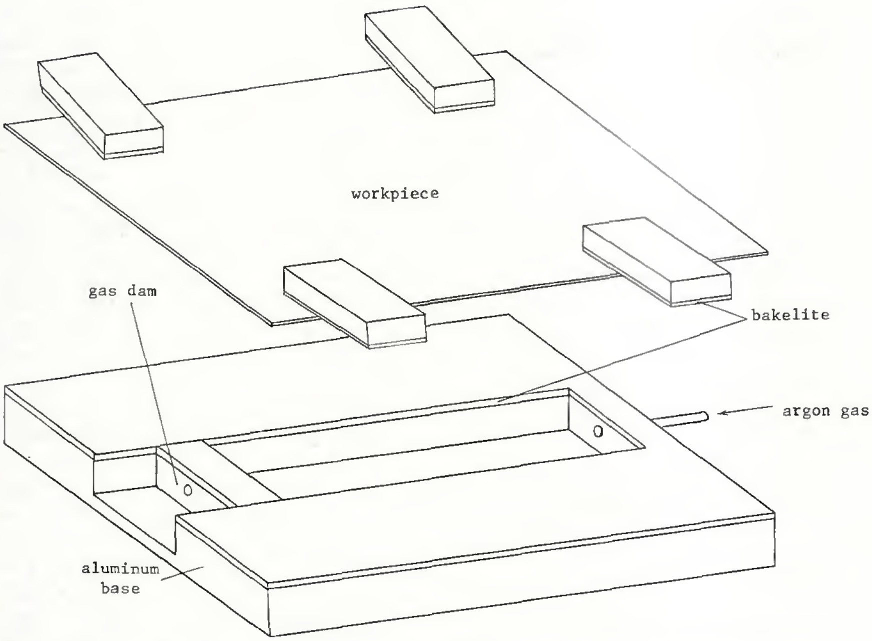

Fig. 4 — The fixtures used for the welding of thin aluminum plates. Both the top of the aluminum base and the bottoms of the clamps were thermally insulated with bakelite to avoid heat sinks during welding. The basin of the bottom fixture was to provide the bottom inert gas for protecting the weld metal from oxidation and for preventing the weld metal from sagging

6061, 5052, 2014 and 7075 were employed in this study. The dimensions of the plates were 200 × 130 × 1.6 mm (8 × 5 × 1/16 in.). Oxides were polished off the surfaces of the plate. The polished surfaces were then cleansed with acetone before welding.

In order to protect the weld metal from oxidation and also prevent the liquid pool from sagging, a special type of fixture was designed. Shown in Fig. 4 is a sketch of the fixture. Argon gas was introduced into the basin of the bottom fixture, and a gas dam was used to hold the gas inside the basin. A hole was drilled through the dam to provide the outlet for the thermocouple wires. Furthermore, in order to avoid heat sinks during welding, both the top of the aluminum base and the bottom of the steel clamps were thermally insulated with bakelite.

A programmable power source was used in conjunction with a traversing carriage of adjustable travel speeds for the welding of the plate. DCRP GTA welding was used to produce bead-on-plate, full-penetration welds, with essentially parallel fusion boundaries in the thickness direction of the plate. All welds were made using argon shielding gas and a 2.4 mm (3/32 in.) tungsten-2% thoria electrode with a balled end of 4 mm (0.16 in.) diameter.

During the early stage of experiment, slight buckling of aluminum plates was found to change the arc voltage rather significantly. As a result of the nonuniform heat input during welding, nonuniform bead widths were encountered frequently. Therefore, in order to maintain a constant arc voltage during welding, an automatic arc voltage control system was employed.

Figure 5 shows the welding equipment hooked up with the arc voltage control system. The welding torch, instead of being attached directly to the traversing carriage, was fixed to the drive unit of the control system. The electrode was connected to the torch sense lead of the drive unit, while the plate was connected to the ground sense lead of the same unit. With the help of the voltage control unit, the arc voltage during welding was maintained within ± 0.1 volt (v) of predetermined values. The welding current, on the other hand, varied less than 1% during all welding experiments. The welding power input was, therefore, very accurately controlled and very reproducible in the present study.

Thermal measurements were conducted by using a high speed, oscillograph-type multiple-channel recorder. In order to minimize their interference with the heat flow during welding, thermocouple wires of 0.13 mm (5/1000 in.) diameter were used. The tips of the thermocouple were planted into small holes of 0.60 mm (0.024 in.) diameter, which were drilled at the predetermined positions of the bottom surface of the plate. These holes were then sealed tightly against the tips of the thermocouples mechanically to ensure good thermal contact.

After welding the weld beads were etched macroscopically to reveal the fusion zone structure. The observed thermal cycles, widths of the fusion zone and weld microstructures were compared with the calculated results of the heat flow model.

Results and Discussion

Thermal Cycles and Widths of the Fusion Zone

The experimental work in the present study is unique in that temperature measurements were conducted inside, as well as outside, the fusion zone. It is to be noted that temperature measurements inside the fusion zone provide the information regarding the degree of convection in the liquid pool. This is important not only for the study of the weld pool solidification, but also for the simulation of heat flow during welding.

It can be expected that, with the same heat input, if the effective liquid conductivity used in the heat flow simulation is too high, the calculated thermal cycle for a point located inside the fusion zone will tend to indicate both too flat a peak and too low a peak temperature. On the other hand, if the effective liquid conduc-

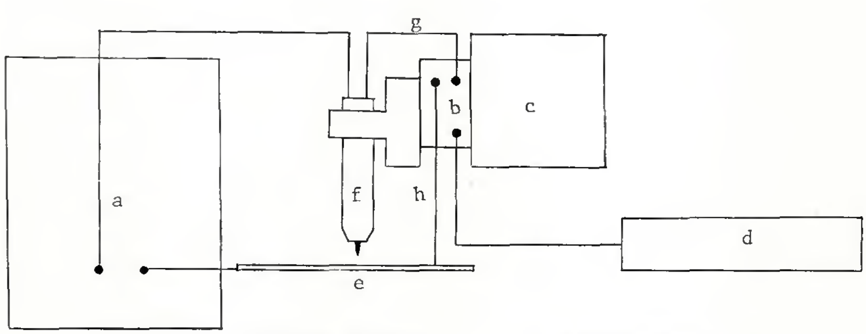

Fig. 5 — The GTA welding system hooked up with an automatic arc voltage control system. The drive unit moved the torch up and down and the control unit maintained the voltage drop across the arc gap within ± 0.1 V of the desired value

RESEARCH/DEVELOPMENT/RESEARCH/DEVELOPMENT/RESEARCH/DEVELOPMENT/RESEARCH/DEVELOPMENT/RESEARCH/DEVELOPMENT

Fig. 6 — The fusion zone macrostructure in 6061 aluminum, plate #14. The columnar grains curved in the welding direction

tivity is too low, both too steep a peak and too high a peak temperature will be obtained.

In the following, the experimental results are presented and compared with the calculated ones for each alloy system. The dimensionless distance, instead of the dimensionless time, was used in the presentation of thermal cycles. This was because the dimensionless distance could be readily converted into the dimensionless time. Therefore, it is unnecessary to introduce one extra dimensionless variable.

It was also found during the heat flow simulation that the surface heat loss during the welding of aluminum alloys was very small and, therefore, was neglected for practical purposes. Furthermore, since the specific heat of the solid phase is very close to that of the liquid phase for aluminum alloys, the dimensionless specific heat C* was set equal to one in the heat flow simulation. Finally the size of the arc at the workpiece surface observed in this study was between 12 (0.47 in.) and 13 mm (0.52 mm) in diameter. According to Pavelic (Ref. 10), the arc heat distribution can be approximated with a Gaussian type distribution function. This was adopted in the present study.

6061 Aluminum. Shown in Fig. 6 is the fusion zone macrostructure of 6061 aluminum, plate #14. The current used was 58.5 amperes (A), the voltage drop across the arc 17.5 V and the welding velocity 4.31 mm/s (10.2 ipm). As can be seen in Fig. 6, the columnar grains curved in the welding direction and the width of the fusion zone was about 7 mm (0.28 in.).

The thermal cycles and the width of the fusion zone, both measured and calculated, are shown in Fig. 7. The dashed lines indicate the experimental results and the solid lines the calculated ones. The values of the dimensionless variables used in the calculation are also listed. The dimensionless heat input Q* = 3.65 corresponded to about 53% of the heat generated at the arc, i.e., the current times the voltage drop measured across the arc gap (not the overall voltage indicated on the voltmeter of the welding machine). This rather low efficiency was perhaps due to the reverse polarity and the shape of the electrode used.

When Rosenthal's solution was used, a 46% efficiency was required in order to match the measured width of the fusion zone, while a 47% efficiency was required to match the measured thermal cycle outside the fusion zone, i.e., at y* = 0.52. The dimensionless conductivity k*, on the other hand, corresponded to an effective liquid conductivity twice the conductivity of the solid phase, indicating significant effects of the weld pool convection. As can be seen, the calculated thermal cycles showed very good agreement with the experimentally mea-

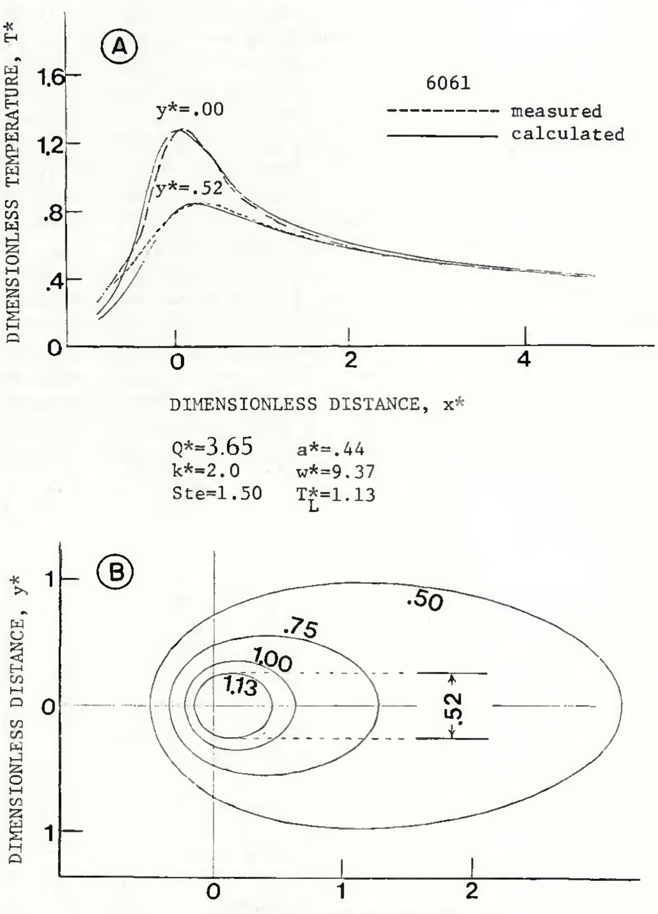

Fig. 7 — Calculated and measured thermal cycles, isotherms and widths of the fusion zone for 6061 aluminum, plate #14. The dashed lines are the experimental results and the solid lines the calculated results. The number indicated on each isotherm is the dimensionless temperature

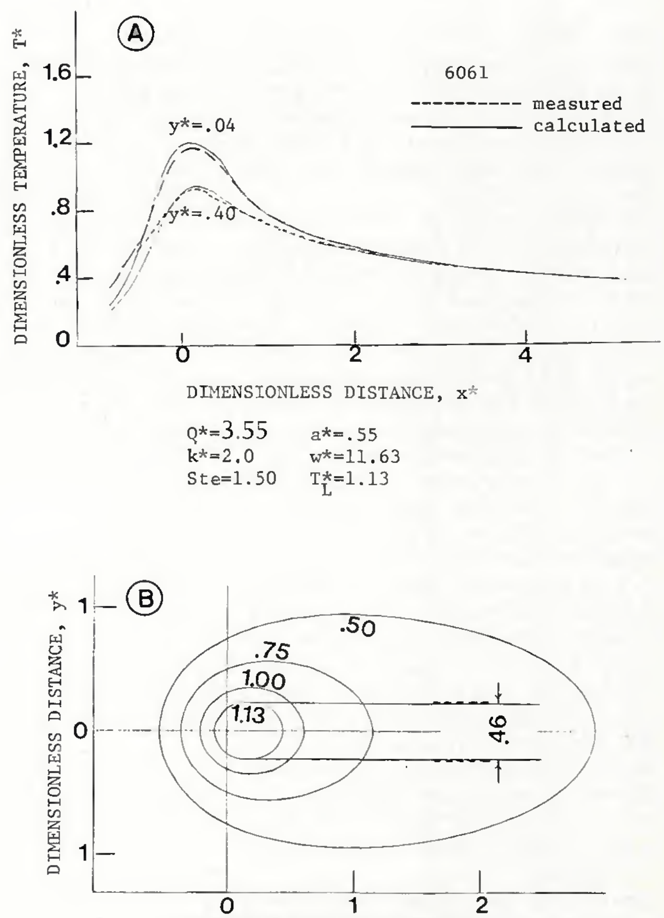

Fig. 8 — Calculated and measured thermal cycles, isotherms and widths of the fusion zone for 6061 aluminum, plate #21. The dashed lines are the experimental results and the solid lines the calculated results. The number indicated on each isotherm is the dimensionless temperature

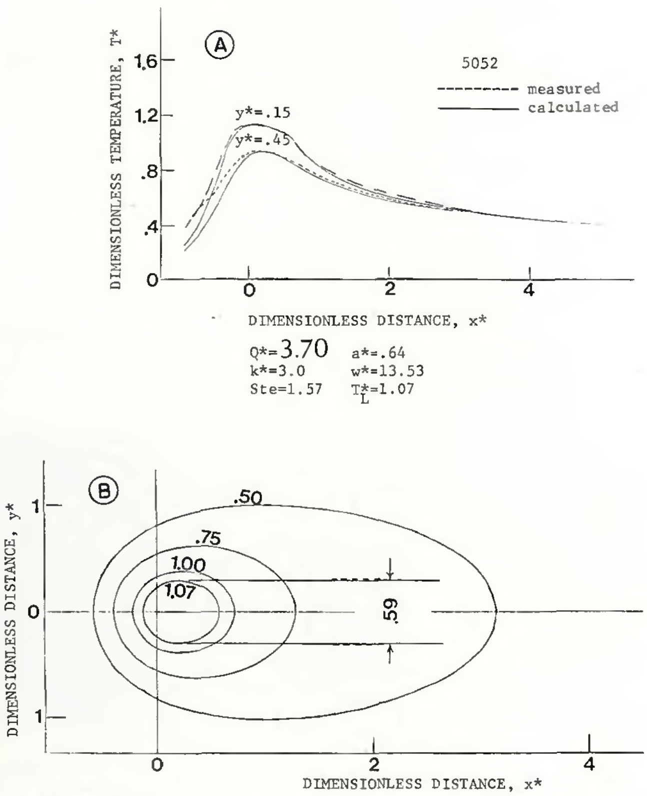

Fig. 9 — Calculated and measured thermal cycles, isotherms and widths of the fusion zone for 5052 aluminum, plate #22. The dashed lines are the experimental results and the solid lines the calculated results. The number indicated on each isotherm is the dimensionless temperature

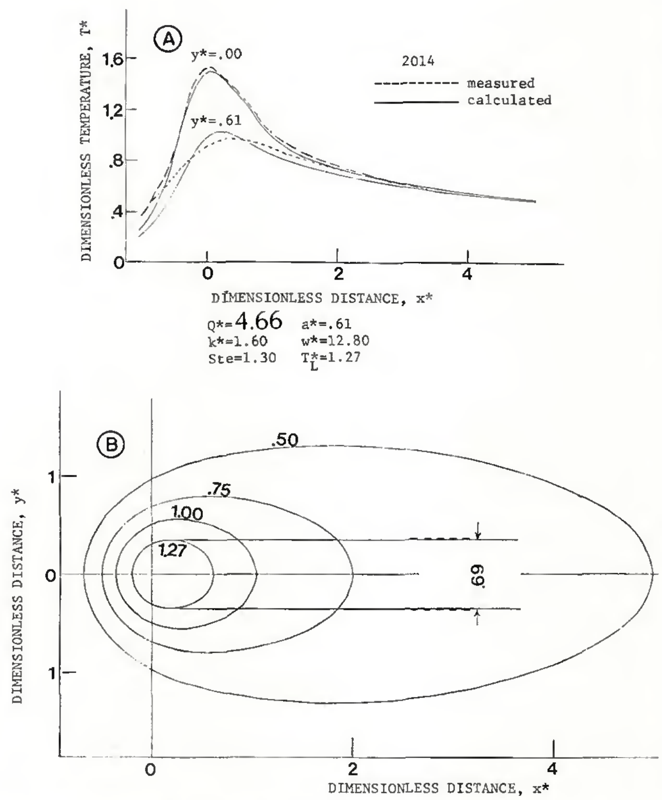

Fig. 10 — Calculated and measured thermal cycles, isotherms and widths of the fusion zone for 2014 aluminum, plate #25. The dashed lines are the experimental results and the solid lines the calculated results. The number indicated on each isotherm is the dimensionless temperature

Table 1—Physical Properties of Materials Used (Ref. 14)

Materials	Liquidus temperature, °C	Solidus[(a)] temperature, °C	Thermal conductivity, watts/m°C	Density, kg/m^3
6061	652	582	168	2700
5052	649	607	139	2680
2014	638	507	155	2800
7075	635	477	130	2740

(a) This is the lower bound of the freezing range.

sured ones.

Figure 7B shows the calculated isotherms, including the liquidus isotherm $T^* = T_L^*$, i.e., the weld pool. The measured width of the fusion zone in this case was exactly the same as the calculated one.

The welding condition of 6061, plate #21, was the same as that of #14, except that the travel speed was increased about 25%. As a result of such an increase, the dimensionless radius of the heat source and the dimensionless width of the plate both increased 25%. As can be seen in Fig. 8, a decrease in both the dimensionless peak temperatures and the dimensionless width of the fusion zone was observed, both experimentally and theoretically. Again, the agreement between the experimental and the calculated results was very good. The dimensionless heat input Q* here was slightly lower than that of plate #14. The reasons for such a slightly lower efficiency are not exactly clear.

5052 Aluminum. The welding condition of 5052 aluminum, plate #22, was the same as that of 6061, plate #21. The thermal cycles and width of the fusion zone are shown in Fig. 9.

As shown in Table 1 (Ref. 14), the freezing range of 5052 is only about 60% that of 6061, giving a dimensionless liquidus temperature T_L^* as low as 1.07. The combination of a lower T_L^* and a slightly higher Q* resulted in a greater dimensionless width of the fusion zone — Fig. 9B.

It is interesting to note that the thermal cycle at y* = 0.15, which is inside the fusion zone, shows a rather flat "peak". This implies that the temperature in the liquid pool was rather uniform, due to the presence of a rather rigorous liquid convection. This point was confirmed by the fact that a higher effective liquid conductivity, i.e., k* = 3.0, did reproduce such a flat "peak".

2014 Aluminum. The welding condition of 2014 aluminum, plate #25, was also the same as that of 6061, plate #21. The thermal cycles and the width of the fusion zone are shown in Fig. 10. Both the thermal conductivity k_s and the solidus isotherm T_s are lower than that of 6061, thus giving a significantly higher dimensionless heat input Q*. This, together with a somewhat lower dimensionless conductivity k*, resulted in significantly higher dimensionless peak temperatures, as shown in Fig. 10A. Although, due to the significantly wider freezing range, the dimensionless liquidus temperature T_L^* appears to be significantly higher than that of 6061. Also, the effect of the higher dimensionless heat input Q* was apparently dominating, since the dimen-

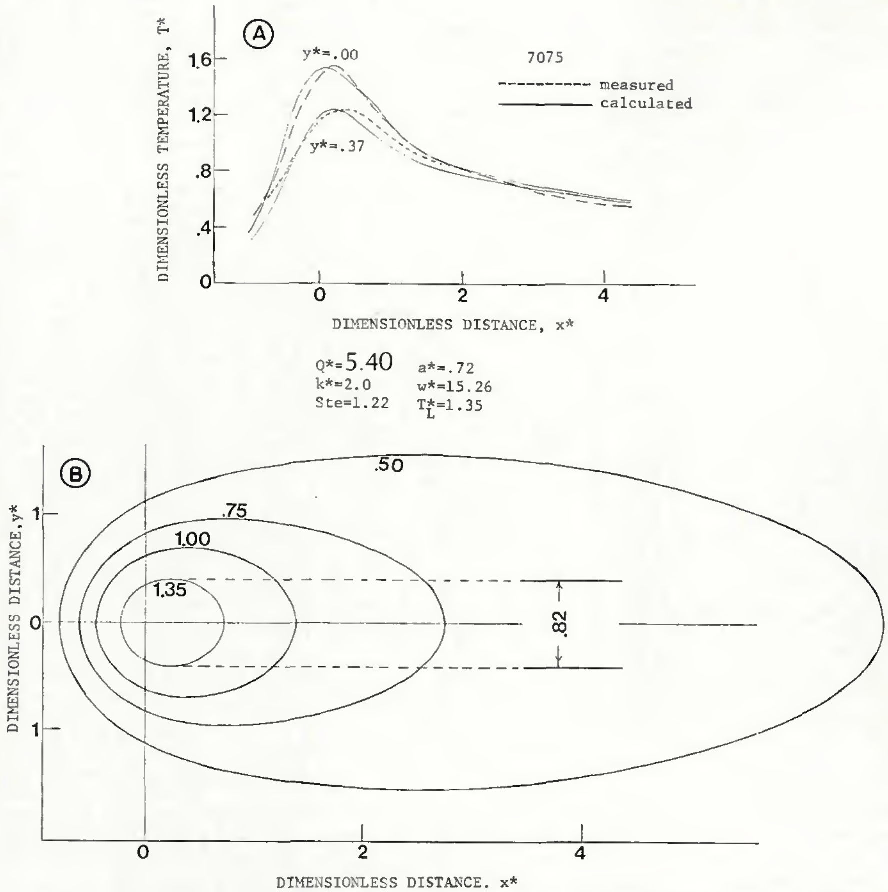

Fig. 11 — Calculated and measured thermal cycles, isotherms and widths of the fusion zone for 7075 aluminum, plate #24. The dashed lines are the experimental results and the solid lines the calculated results. The number indicated on each isotherm is the dimensionless temperature

Table 2—Comparison Between the Measured and the Calculated Dimensionless Widths of the Fusion Zone

Material	Dimensionless Width of Fusion Zone	
	Measured	Calculated
2014	.71	.69
5052	.60	.59
6061	.52	.52
6061	.48	.46
7075	.82	.82

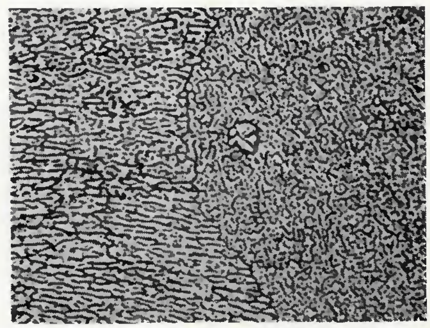

Fig. 12 — Transverse microstructure near the weld center line of 6061 aluminum, plate #14. X200 (reduced 52% on reproduction)

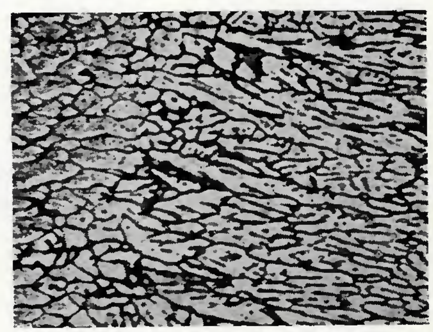

Fig. 13 — Transverse microstructure at the fusion line in 6061 aluminum, plate #14. Coarser cells in the fusion zone (than in Fig. 12) are evident. X200 (reduced 52% on reproduction)

sionless width of the fusion zone was still significantly greater than that of 6061.

7075 Aluminum. The welding condition of 7075 aluminum, plate #24, was also the same as that of 6061, plate #21. The measured thermal cycles and width of the fusion zone are shown in Fig. 11. Due to the significantly lower thermal conductivity k_s and solidus temperature T_s, a much higher dimensionless heat input Q* than that of 6061 was obtained. Therefore, as expected, significantly higher dimensionless peak temperatures and greater dimensionless width of the fusion zone were observed.

The calculated and the measured widths of the fusion zone are summarized in Table 2. As can be seen, the agreement was very good. It is interesting to note that, when Rosenthal's equation was used, the measured thermal cycle and width of the fusion zone could not both be matched at the same time. In fact, when the width of the fusion zone was matched, calculated peak temperatures in the heat affected zone as much as 20% off the measured ones were found in some cases. On the other hand, with the peak temperatures in the heat-affected zone matched, the calculated widths of the fusion zone were sometimes more than 30% off the measured ones.

The worst of all was, of course, at the weld center line, where Rosenthal's calculation yielded infinitely high peak temperatures, while the experimental results indicated only finite values.

Microstructures

In addition to the results presented and discussed above, the weld microstructure was also examined. However, due to the limitation of space, only the results of 6061 aluminum, plate #14, will be discussed here. Figures 12 to 14 show the microstructures of the transverse cross-section of the weld, from near the centerline to the outside of the fusion zone.

The large grain appearing on the right hand side of the micrograph shown in Fig. 12 was close to the weld center line. It was one of the axial columnar grains shown in Fig. 6. The grain that appeared on the left hand side of the micrograph was another columnar grain which was growing toward the weld centerline and was blocked by the other grain. The relatively small cell spacings shown in this micrograph suggest that the cooling rate through the solidification range was fairly high (Ref. 15).

Figure 13, on the other hand, suggests significantly greater cell spacings and hence lower cooling rate near the fusion line of the weld. This is consistent with the calculation of the heat flow model. In fact, the calculated average cooling rate was 124°C/s (223°F/s) at the weld center line and was 44°C/s (79°/s) at the fusion line. The cell sizes for such cooling rates compare very favorably with the established cell size vs. cooling rate relationship for commercial aluminum alloys (Ref. 15), indicating quantitative agreement between the heat flow calculations and the microstructure observed.

It is to be noted that the cooling rates, whether calculated with the heat flow model or estimated from the observed

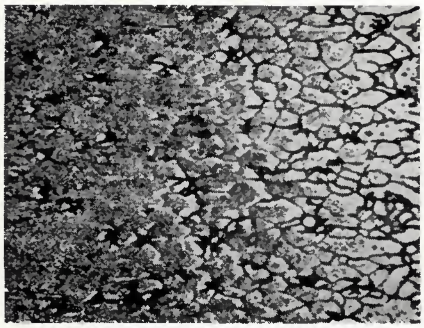

Fig. 14 — Transverse microstructure near the fusion line (outside the fusion zone) in 6061 aluminum alloy, plate #14. X200 (reduced 52% on reproduction)

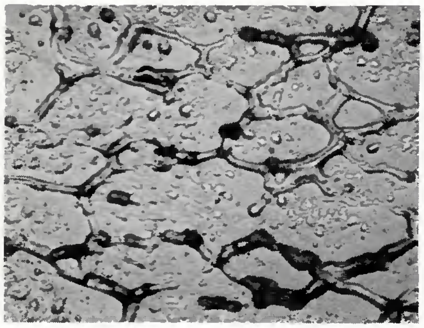

Fig. 15 — Transverse microstructure near the fusion line (outside the fusion zone) in 6061 aluminum alloy, plate #14. The melting of eutectic materials along the grain boundaries and inside the grains is clearly visible. X800 (reduced 52% on reproduction)

cell sizes, seem lower than what would have been expected in welding. This, however, is not surprising. Since, due to the high thermal conductivity of aluminum, the strong convection of the weld pool and the slow welding velocity used, the temperature gradients were not very high. Also, thin plates are much worse heat sinks than thick plates and, therefore, cool down weld beads much more slowly.

Finally, Fig. 14 shows the microstructure near the fusion zone. The calculated peak temperatures in this area were above the solidus temperature, thus suggesting the remelting of eutectic materials. Figure 15, which shows the microstructure of the same area at a higher magnification, does indicate such remelting along the grain boundaries and inside the grains.

Conclusions

The most important conclusions are:

1. The arc voltage controller maintained a very constant arc voltage across the arc gap, giving a very accurately controlled arc heat input regardless of the distortion tendency of thin aluminum plates during welding.
2. Thermal measurements inside the fusion zone provided valuable information concerning the degree of weld pool convection.
3. Rosenthal's analytical solution showed fair agreement with the experimental results, except in weld pools.
4. The experimentally observed thermal cycles, widths of the fusion zone and weld microstructures agreed very well with those calculated with the heat flow model developed. Therefore, such a heat flow model can be used to study both solidification and solid-state phase transformations during thin-plate welding.

Acknowledgments

The authors gratefully acknowledge support for this study from the National Science Foundation under the Research Initiation Grant (DMR-8007315) and from the Center for the Joining of Materials at Carnegie-Mellon University, under NSF Grant DMR-7824699. They would also like to give thanks to the Aluminum Company of America for supplying the aluminum plates. Finally, the assistance of Mr. Yi-Ping Le in the experimental work is greatly appreciated.

References

1. Rosenthal, D. 1941. Mathematical theory of heat distribution during welding and cutting. *Welding Journal* 20(5): 220-s to 234-s.
2. Hess, W. F.; Merrill, L. L.; Nippes, Jr., E. F.; and Bunk, A. P. 1943. The measurement of cooling rates associated with arc welding and their application to the selection of optimum welding conditions. *Welding Journal,* 22(9): 377-s to 422-s.
3. Rykalin, N. N. 1957. *Calculation of heat processes during welding.* Berlin: VEB-Verlag Technik.
4. Myers, P. S.; Uyehara, O. A.; and Borman, G. L. 1967 (July). *Fundamentals of heat flow in welding.* Welding Research Council Bulletin, No. 123.
5. Grosh, R. J.; Trabant, E. A.; and Hawkins, G. A. 1955. Temperature distribution in solids of variable thermal properties heated by moving heat sources. *Quart. Appl. Math.* 13: 161-167.
6. Swift-Hook, D. T., and Gick, A. E. F. 1973. Penetration welding with lasers. *Welding Journal* 52(11): 492-s to 499-s.
7. Jhaveri, P.; Moffatt, W. G.; and Adams, Jr., C. M. 1962. The effect of plate thickness and radiation on heat flow in welding and cutting. *Welding Journal* 41(1): 12-s to 16-s.
8. Ghent, H.; Hermance, C. E.; Kerr, H. W.; and Strong, A. B. 1979. Heat conduction modeling of two dimensional TIG weld pools, *Arc physics and weld pool behavior.* Conference Proceedings. Cambridge, U.K.: The Welding Institute.
9. Trivedi, R., and Srinivason, S. R. 1974. Temperature distribution around a moving cylindrical source. *Journal of Heat Transfer.* Trans. of the ASME 96: 427-428.
10. Pavelic, V.; Tanbakuchi, R.; Uyehara, O. A.; and Myers, P. S. 1969. Experimental and computed temperature histories in gas tungsten arc welding of thin plates. *Welding Journal* 48(7): 295-s to 305-s.
11. Friedman, E. 1975. Thermomechanical analysis of the welding process using the finite element method. *Journal of Pressure Vessel Technology* 97J: 206-213. Trans. ASME.
12. Sharir, Y.; Grill, A.; and Pelleg, J. 1980. Computation of temperatures in thin tantalum sheet welding. *Metallurgical Transactions* 11B: 257-265.
13. Kou, S. 1981. Simulation of heat flow during the welding of thin plates. Submitted to *Met. Trans. B.*
14. Aluminum Association. 1976. *Aluminum Standards and Data.*
15. Flemings, M. C. 1974. *Solidification processing,* McGraw-Hill.